

Structural insight into selectivity and resistance profiles of ROS1 tyrosine kinase inhibitors

Monika A. Davare^{a,b,1}, Nadeem A. Vellore^{c,d,1}, Jacob P. Wagner^{a,b,1}, Christopher A. Eide^{e,f,1}, James R. Goodman^e, Alexander Drilon^g, Michael W. Deininger^{c,d}, Thomas O'Hare^{c,d,2,3}, and Brian J. Druker^{e,f,2,3}

^aKnight Cancer Institute, Oregon Health & Science University, Portland, OR 97239; ^bDepartment of Pediatrics, Oregon Health & Science University, Portland, OR 97239; ^cHuntsman Cancer Institute, The University of Utah, Salt Lake City, UT 84112; ^dDivision of Hematology and Hematologic Malignancies, The University of Utah, Salt Lake City, UT 84112; ^eDivision of Hematology and Medical Oncology, Knight Cancer Institute, Oregon Health & Science University, Portland, OR 97239; ^fHoward Hughes Medical Institute, Portland, OR 97239; and ^gMemorial Sloan Kettering Cancer Center, New York, NY 10065

Contributed by Brian J. Druker, August 5, 2015 (sent for review April 10, 2015; reviewed by Nicholas Levinson and Ariel Lopez-Chavez)

Oncogenic ROS1 fusion proteins are molecular drivers in multiple malignancies, including a subset of non-small cell lung cancer (NSCLC). The phylogenetic proximity of the ROS1 and anaplastic lymphoma kinase (ALK) catalytic domains led to the clinical repurposing of the Food and Drug Administration (FDA)-approved ALK inhibitor crizotinib as a ROS1 inhibitor. Despite the antitumor activity of crizotinib observed in both ROS1- and ALK-rearranged NSCLC patients, resistance due to acquisition of ROS1 or ALK kinase domain mutations has been observed clinically, spurring the development of second-generation inhibitors. Here, we profile the sensitivity and selectivity of seven ROS1 and/or ALK inhibitors at various levels of clinical development. In contrast to crizotinib's dual ROS1/ALK activity, cabozantinib (XL-184) and its structural analog foretinib (XL-880) demonstrate a striking selectivity for ROS1 over ALK. Molecular dynamics simulation studies reveal structural features that distinguish the ROS1 and ALK kinase domains and contribute to differences in binding site and kinase selectivity of the inhibitors tested. Cell-based resistance profiling studies demonstrate that the ROS1-selective inhibitors retain efficacy against the recently reported CD74-ROS1^{G2032R} mutant whereas the dual ROS1/ALK inhibitors are ineffective. Taken together, inhibitor profiling and stringent characterization of the structure–function differences between the ROS1 and ALK kinase domains will facilitate future rational drug design for ROS1- and ALK-driven NSCLC and other malignancies.

ROS1 | ALK | kinase | inhibitor | structural modelling

Constitutively activated kinase fusion proteins that arise from somatic chromosomal rearrangements are frequent drivers of malignant transformation in cancer and represent a targetable vulnerability for clinical intervention. The clinical success of the tyrosine kinase inhibitor (TKI) imatinib in targeting the oncogenic BCR-ABL1 fusion protein in chronic myeloid leukemia (CML) motivated efforts to identify and target oncogenic kinases in other cancers (1–3). One such setting is non-small cell lung cancer (NSCLC), where chromosomal rearrangements of the receptor tyrosine kinase (RTK) anaplastic lymphoma kinase (ALK) are found in 4–5% of patients (4, 5). The validation of rearranged ALK as an oncogenic driver prompted the discovery and clinical implementation of crizotinib as the first clinical targeted inhibitor for use in ALK fusion-positive NSCLC (6, 7).

Fusion proteins involving the highly related kinase ROS1, an orphan RTK of the insulin receptor family, are present in ~1% of NSCLC patients. ROS1 rearrangements span a variety of fusion partners across several other epithelial malignancies, including cholangiocarcinoma, gastric cancer, and ovarian cancer (4, 8). CD74-ROS1 is the most frequent ROS1 fusion detected in NSCLC. ROS1 fusion proteins are transforming drivers that contribute to tumorigenesis or tumor progression in multiple experimental model systems (9–11).

Approximately 75,000 and 15,000 new NSCLC patients per year are anticipated to harbor tumors driven by rearranged ALK or ROS1, respectively. Although mutually exclusive in a given

tumor and considered to be distinct molecular subgroups (12), patients presenting with ROS1 or ALK fusion-driven lung cancer share clinical features, tend to be younger compared with other NSCLC patients, and have little to no history of smoking. The kinase domains of ROS1 and ALK display a high degree of sequence homology (13), prompting investigation of crizotinib for activity against ROS1 (12). Recent phase I data confirmed significant responses to crizotinib in ROS1-rearranged NSCLC patients (14, 15).

Despite the demonstrated clinical efficacy of TKI-based targeted therapies in cancer, a universal challenge is emergence of drug resistance and ensuing disease progression. Resistance commonly involves either acquisition of kinase domain mutations that compromise inhibitor binding or activation of alternative pathways that provide compensatory cell survival signals. Concordant with previous clinical experience from other TKIs, such as imatinib in CML and erlotinib or gefitinib in lung cancer (16–18), resistance due to acquisition of kinase domain mutations is frequently observed

Significance

Targeting oncogenic ROS1 fusion proteins with crizotinib has shown promising clinical outcomes in non-small cell lung cancer (NSCLC) patients, but emergence of resistance to therapy has been reported. By profiling the activity of clinically viable ROS1/anaplastic lymphoma kinase (ALK) inhibitors, we discovered that the Food and Drug Administration (FDA)-approved inhibitor cabozantinib potentially inhibits native ROS1 and the crizotinib-resistant ROS1^{G2032R} mutant, suggesting potential utility for treatment of ROS1-rearranged lung cancer. Notably, cabozantinib is ineffective against the closely related ALK kinase. Molecular modeling shows specific structural differences between the kinase domains of ROS1 and ALK that explain selective binding of cabozantinib to ROS1. These findings reveal limitations pertaining to the widely presumed inhibitory reciprocity of ROS1 and ALK inhibitors and may facilitate rational design of new ROS1-selective inhibitors.

Author contributions: M.A.D., N.A.V., C.A.E., T.O., and B.J.D. designed research; M.A.D., N.A.V., J.P.W., C.A.E., and J.R.G. performed research; M.A.D., N.A.V., and J.P.W. contributed new reagents/analytic tools; M.A.D., N.A.V., J.P.W., C.A.E., and T.O. analyzed data; and M.A.D., N.A.V., C.A.E., A.D., M.W.D., T.O., and B.J.D. wrote the paper.

Reviewers: N.L., University of Minnesota; and A.L.-C., University of Miami.

Conflict of interest statement: The Oregon Health & Science University has clinical trial contracts with Novartis and Bristol-Myers Squibb (BMS) to pay for patient costs, nurse and data manager salaries, and institutional overhead. B.J.D. does not derive salary, nor does his laboratory receive funds, from these contracts. M.W.D. served on advisory boards and as a consultant for BMS, ARIAD, and Novartis.

Freely available online through the PNAS open access option.

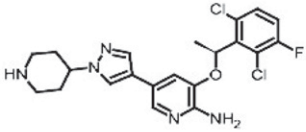
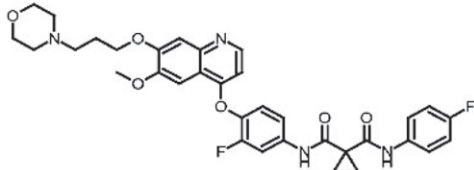
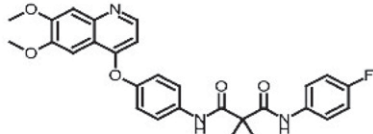
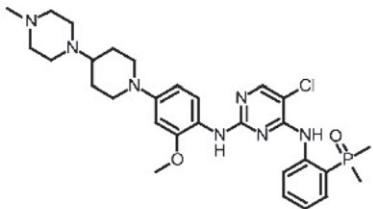
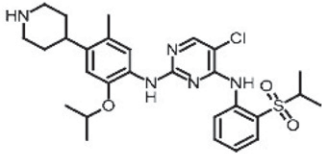
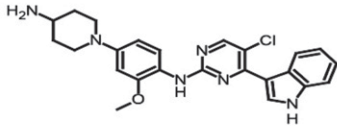
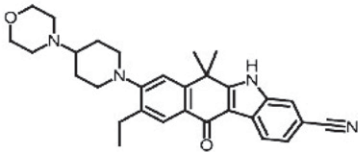
¹M.A.D., N.A.V., J.P.W., and C.A.E. contributed equally to this work.

²T.O. and B.J.D. contributed equally to this work.

³To whom correspondence may be addressed. Email: drukerb@ohsu.edu or thomas.ohare@hci.utah.edu.

This article contains supporting information online at www.pnas.org/lookup/suppl/doi:10.1073/pnas.1515281112/-DCSupplemental.

Table 1. Summary of ALK and ROS1 tyrosine kinase inhibitors in clinical development

Inhibitor	Chemical structure	Clinical development status in United States	ALK or ROS1 clinical resistance mutations reported to date	
			ALK	ROS1
Crizotinib		FDA approved (ALK-positive NSCLC)	1151T-ins L1152R C1156Y I1171T F1174(LV)	L1196M G1202R S1206Y G1269(A/S)
Foretinib		Phase II	Not yet evaluated	Not yet evaluated
Cabozantinib		FDA approved (medullary thyroid carcinoma)	Not yet evaluated	None yet reported
Brigatinib (AP26113)		FDA breakthrough drug approval (crizotinib-resistant or -intolerant ALK-positive NSCLC)	None yet reported	None yet reported
Ceritinib (LDK-378)		Accelerated FDA approval (crizotinib-resistant or -intolerant ALK-positive NSCLC)	F1174(CV) G1202R	None yet reported
AZD3463		Preclinical	Not yet evaluated	Not yet evaluated
Alectinib (CH54248020)		FDA breakthrough drug approval (crizotinib-resistant or -intolerant ALK-positive NSCLC)	I1171(N/S/T) G1202R	Not yet evaluated

in crizotinib-treated NSCLC patients harboring *ALK* fusions (7, 19–21). This experience has prompted the development of several second-generation ALK inhibitors capable of circumventing resistance. Furthermore, compared with *ALK*-rearranged lung cancers, *ROS1*-rearranged cancers are less frequent, and clinical benefit with crizotinib may be more durable. The median progression-free survival for crizotinib-treated patients from phase I evaluation of *ROS1*-rearranged NSCLC is 19.2 mo (15), compared with 7.7 mo for patients with *ALK*-rearranged disease (phase III data) (14). Given these factors, mechanisms of acquired resistance to crizotinib in the clinic may take longer to identify, and only the CD74-*ROS1*^{G2032R} mutation has been reported to date (22).

We have previously reported that foretinib (XL-880) is a potent *ROS1* inhibitor that retains efficacy against the crizotinib-resistant CD74-*ROS1*^{G2032R} mutant in cell-based assays (23). In contrast to crizotinib's dual *ROS1*/*ALK* efficacy, we observed that foretinib is a poor *ALK* inhibitor. These findings establish that not all *ROS1* inhibitors possess inhibitory reciprocity for *ALK*, and drug discovery efforts that use one kinase as a proxy for the other may face limitations.

Here, we report *in vitro* profiling of a panel of clinically relevant *ROS1* and *ALK* inhibitors. To complement cell-based resistance profiling of *ROS1*-selective inhibitors, structural comparison of the kinase domains of *ROS1* and *ALK* and computational modeling of TKI binding to native and mutant kinase domains were

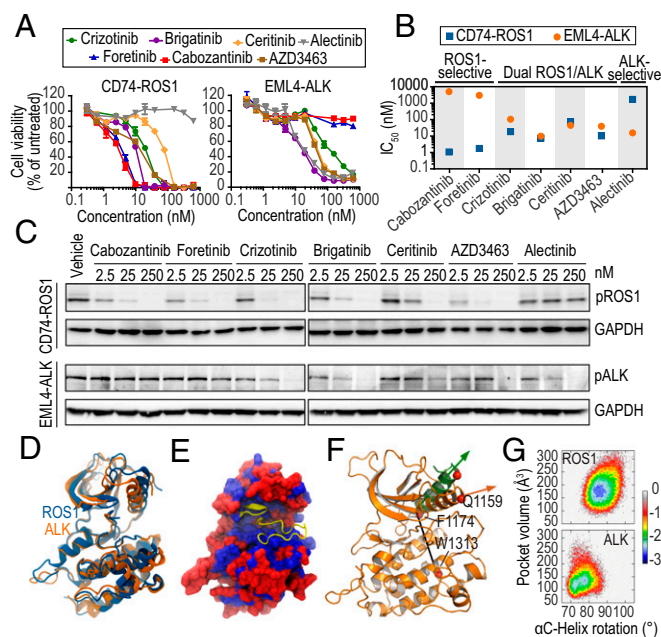


Fig. 1. Structural differences between the ROS1 and ALK kinase domains underlie the differential selectivity of TKIs. (A) Proliferation of Ba/F3 CD74-ROS1 and EML4-ALK cells after 72-h exposure to cabozantinib, foretinib, crizotinib, brigatinib, ceritinib, AZD3634, and alectinib. Data are normalized to vehicle-treated control, and values shown are the mean \pm SEM. (B) Scatter plot of cell proliferation IC_{50} values for each TKI against Ba/F3 cells expressing CD74-ROS1 (blue) and EML4-ALK (orange). Categories of selectivity profile are indicated above the plot. (C) Immunoblot analysis of phospho-ROS1 from TKI-treated Ba/F3 CD74-ROS1 cells (Upper) and phospho-ALK from TKI-treated Ba/F3 EML4-ALK cells (Lower). (D) Alignment of ROS1 (blue) and ALK (orange) using structural homology (based on α atoms). The A-loop is not shown. (E) Surface representation of ROS1 kinase, with P- and A-loops shown in ribbon representation (yellow). The protein surface is colored based on sequence identity between ROS1 and ALK kinase, with red for identical sequence and blue for nonidentical sequence. (F) Ribbon model depicting the rotation of α C-helix in ROS1 and ALK. (G) α C-helix rotation plotted against the volume of the specificity site for ROS1 and ALK kinase calculated from molecular dynamic simulation.

also performed. These results provide insights into therapeutically exploitable structural differences between ROS1 and ALK that impact inhibitor binding and design.

Results

In Vitro Profiling Reveals Differences in TKI Selectivity for ROS1 Versus ALK. Given the clinical success with crizotinib in ALK fusion-driven NSCLC and the fact that the ROS1 and ALK kinase domains display high sequence homology, there is an operating assumption that ALK inhibitors can be repurposed as ROS1 inhibitors (13). However, comprehensive sensitivity profiling of first- and second-generation ALK inhibitors against native and crizotinib-resistant ROS1 has not been undertaken. We screened a panel of seven TKIs at varying stages of clinical development (Table 1) against Ba/F3 cells transformed with CD74-ROS1 or EML4-ALK. Cabozantinib and foretinib both demonstrated a high degree of selectivity for ROS1 compared with ALK, potently inhibiting the growth of CD74-ROS1 cells (IC_{50} of 1.1 nM and 1.8 nM, respectively) while exhibiting minimal effect on EML4-ALK cells at the highest concentration tested (2,500 nM) (Fig. 1A). Conversely, although Ba/F3 EML4-ALK cells were confirmed to be sensitive to inhibition by alectinib (IC_{50} of 12.3 nM), CD74-ROS1 cells were alectinib-insensitive (IC_{50} of 1,950 nM). The remaining TKIs [crizotinib, brigatinib (formerly AP26113), ceritinib, AZD3463] exhibited varying levels of inhibition for CD74-ROS1 and EML4-ALK cells, with brigatinib and AZD3463 displaying near equi-

potency for both (IC_{50} of 7.5 vs. 9.8 nM and 10.2 vs. 39.4 nM, respectively) (Fig. 1A). These results establish three categories with respect to ROS1 and ALK inhibitor selectivity: ROS1-selective (cabozantinib, foretinib), dual ROS1/ALK (crizotinib, brigatinib, ceritinib, AZD3463), and ALK-selective inhibitors (alectinib) (Fig. 1B and Table S1).

Consistent with findings from cell proliferation assays, immunoblot analysis after short-term treatment of Ba/F3 CD74-ROS1 cells with ROS1-selective and dual ROS1/ALK TKIs demonstrated concentration-dependent effects on ROS1 tyrosine phosphorylation (Y2274) (Fig. 1C). Furthermore, although significant inhibition of ALK tyrosine phosphorylation (Y1278) occurred in a concentration-dependent manner in Ba/F3 EML4-ALK cells treated with ALK-selective and dual ROS1/ALK TKIs, cabozantinib and foretinib did not reduce ALK phosphorylation at concentrations up to 250 nM (Fig. 1C). Comparable selectivity findings were observed in the human NSCLC cell lines HCC78 and H3122, which harbor native SLC-ROS1 and EML4-ALK fusions, respectively. Downstream effector pathways (MAPK and AKT) activated by oncogenic ROS1 and ALK were also suppressed in a concentration-dependent manner (Fig. S1). These data imply structural differences between the ROS1 and ALK kinase domains that dictate selectivity and efficacy of TKI binding.

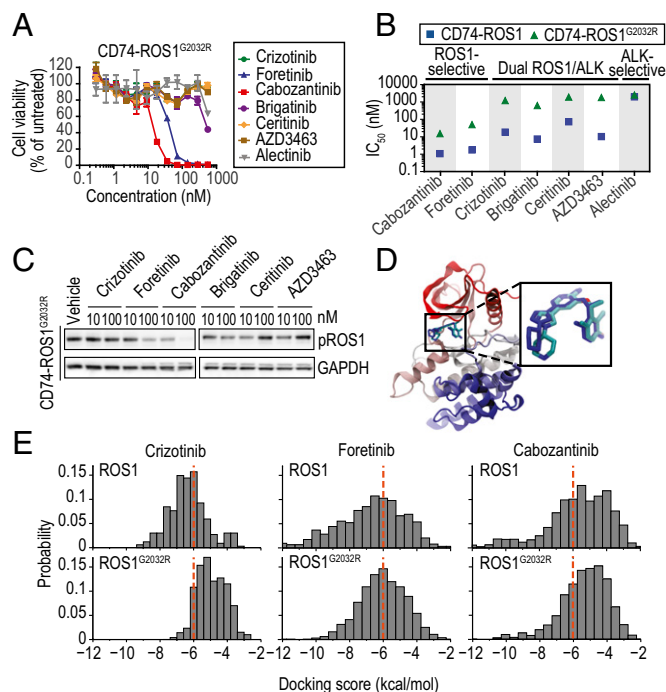


Fig. 2. ROS1-selective TKIs retain efficacy against the crizotinib-resistant ROS1^{G2032R} mutant. (A) Dose-response curves for proliferation of Ba/F3 CD74-ROS1^{G2032R} cells after 72-h exposure to varying concentrations of cabozantinib, foretinib, crizotinib, brigatinib, ceritinib, AZD3634, and alectinib. Data are normalized to vehicle-treated cells, and values shown are the mean \pm SEM. (B) Scatter plot of cell proliferation IC_{50} values for each of the indicated TKIs against Ba/F3 cells expressing native CD74-ROS1 (blue) and CD74-ROS1^{G2032R} (green). Categories of selectivity profile are indicated above the plot. (C) Immunoblot analysis of phospho-ROS1 from Ba/F3 CD74-ROS1^{G2032R} cells after treatment with the indicated TKIs. (D) Overlay of crizotinib docking from simulated models with the actual ROS1:crizotinib complex. (E) Docking score histograms for native ROS1 and ROS1^{G2032R} for crizotinib, foretinib, and cabozantinib. A threshold docking score of -6 is indicated by the vertical dashed orange line, where scores above or below this value correspond to poor or good binding conformations, respectively.

Structural Differences in the Kinase Domains of ROS1 and ALK Underlie TKI Selectivity. ROS1 and ALK share >64% overall sequence homology in the kinase domain and ~84% within the ATP binding site. Structural alignment (Fig. 1D and Fig. S2) demonstrated a low overall root mean square deviation (rmsd) of 2.3 Å between the two kinase domains. However, in comparison with the ATP binding site, the specificity site (defined as the pocket enclosed between the α C-helix and the catalytic DFG loop) (Fig. S3A) in ALK and ROS1 showed multiple differences (Fig. 1E). To investigate these subtle differences, we performed molecular dynamics (MD) simulations of the ROS1 and ALK kinase domains for 500 ns under explicit solvent conditions using the catalytically active and inactive conformations. Throughout this manuscript, “active” refers to the aspartic acid–phenylalanine–glycine (DFG)-in state and “inactive” refers to the DFG-out state of the kinase, irrespective of the conformation of the rest of the A-loop. Both ROS1 and ALK were stable during the course of the simulation, and no large-scale conformational change was observed (Fig. S2). Root mean square fluctuation (RMSF) of the protein was also measured from the simulation (Fig. S3B). The α C-helix was stable in the active conformation of both ROS1 and ALK whereas flexibility of the P-loop was slightly higher compared with the corresponding inactive conformation. Although MD simulation of the active state of ALK was initialized using the A-loop in the autoinhibitory state, conformations pertaining to the active A-loop were also explored intermittently during the course of MD simulation. Based on the simulations, the A-loop was overall significantly more flexible than the other structural elements of the ROS1 and ALK kinase domains. The active conformation of ALK showed reduced flexibility in the A-loop compared with the inactive conformation due to stabilization through a network of aromatic/hydrophobic residues (Y1096, F1098, F1174, F1245, and F1271) at the specificity site (Fig. S3C). In particular, in the active state of ALK, A-loop residue Y1278 engages in an aromatic stacking interaction with Y1096, which in turn is internally stabilized by four neighboring phenylalanine residues. Conversely, the inactive conformation of ROS1 showed less flexibility in the A-loop compared with the active conformation, largely due to increased proximity of the A-loop to both the P-loop and the α C-helix compared with ALK (Fig. S3D).

Conformational analysis of the specificity site using MD simulations further distinguished the inactive conformations of ROS1 and ALK with respect to pocket volume and α C-helix orientation (Fig. 1F). Specifically, ROS1 and ALK sampled markedly different average pocket volumes (186 Å³ and 135 Å³, respectively) (Fig. 1G), and the positioning of the bulky side-chain of Q2012 in ROS1 close to the C terminus of the α C-helix restricts the α C-helix from collapsing into the specificity site. In contrast, the equivalent position in ALK (C1182) lacks such constraints, thus reducing pocket volume. Also, in ROS1, the proximity of Q2012 to the α C-helix influences local changes and contributes to a backbone hydrogen bond observed between M2001 and E1997 whereas ALK lacks such an interaction. Also, ROS1 and ALK differ in the identity of amino acid sidechains lining the specificity site pocket, providing an additional source of divergence in its size and shape. In particular, ROS1 M2001 and L2010 correspond to ALK I1171 and V1180, respectively. These subtle differences in the specificity site could impact the orientation of the α C-helix, as evidenced by the ROS1 α C-helix sampling an average of 88° compared with 75° in ALK (Fig. 1G).

These findings suggest that, despite the significant sequence homology between ROS1 and ALK, differences in the rigidity and orientation of the α C-helix and A-loop contribute to specificity site pocket volume, with the larger pocket in ROS1 capable of accommodating binding of larger scaffolds.

The CD74-ROS^{G2032R} Mutation Confers Resistance to Dual ROS1/ALK TKIs but Remains Sensitive to the ROS1-Selective Inhibitor Cabozantinib. Emergence of clinical resistance due to acquisition of a G2032R

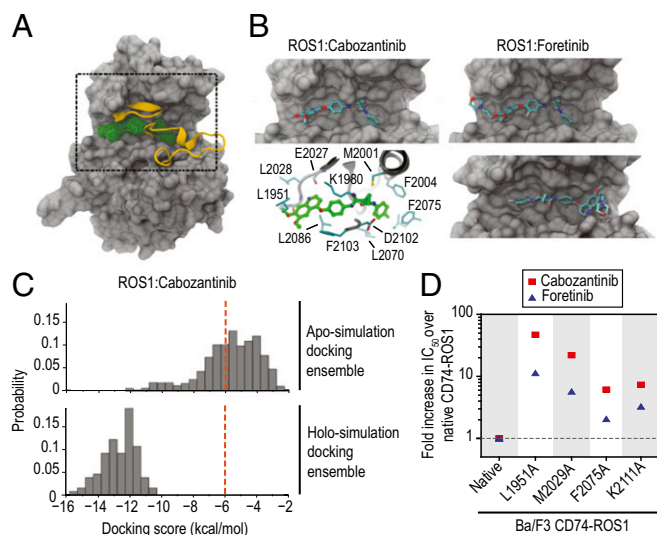


Fig. 3. Structural modeling reveals that the ROS1-selective TKIs cabozantinib and foretinib uniquely bind the inactive conformation of the ROS1 kinase domain. (A) Surface representation of the inactive conformation of ROS1 with the predicted binding of cabozantinib shown as a space-filling mesh (green). The P- and A-loops are shown as ribbons in yellow. (B) Predicted binding poses for cabozantinib and foretinib with inactive ROS1 (Left and Right, respectively). For cabozantinib, a detailed view of specific contact residues is shown (lower left). For foretinib, an alternative, reverse-orientation binding pose is also shown (Lower Right). The P-loop and A-loop are omitted to better illustrate TKI binding. (C) Docking score histograms for the parental conformation docking ensemble and extended, induced-fit conformation docking of cabozantinib to ROS1. (D) Scatter plot showing fold-over-native cell proliferation IC₅₀ values for cabozantinib (blue) and foretinib (red) against Ba/F3 CD74-ROS1 cells with the indicated structurally implicated differentiating residues mutated to alanine substitutions.

mutation in the kinase domain of CD74-ROS1 was recently documented in a crizotinib-refractory NSCLC patient, confirming that TKI vulnerability to kinase domain mutations extends to targeting of ROS1 (15, 22). We ranked TKIs in our panel for the capability to block growth and survival of Ba/F3 CD74-ROS1^{G2032R} cells. We found that cabozantinib, a Food and Drug Administration (FDA)-approved inhibitor structurally related to foretinib (Table 1), is a highly effective inhibitor of CD74-ROS1^{G2032R} and exhibits a fourfold higher potency compared with foretinib (IC₅₀ of 15.3 vs. 50.1 nM) (Fig. 2A). In contrast to the ROS1-selective TKIs, none of the dual ROS1/ALK inhibitors showed efficacy against the CD74-ROS1^{G2032R} mutant, exhibiting ~25- to 140-fold reduced sensitivity compared with cells expressing native CD74-ROS1 (Fig. 2B and Table S1). These trends were confirmed by immunoblotting, where cabozantinib was the most potent inhibitor of ROS1 autophosphorylation in Ba/F3 CD74-ROS1^{G2032R} cells (Fig. 2C).

MD simulation has played a major role in uncovering intricate details of biomolecular recognition at the atomic level (24, 25). To better understand the effect of the G2032R mutation with respect to differential TKI binding, MD simulation of the ROS1^{G2032R} mutant was performed to relax the entire complex. The system was stable over time, and no large-scale conformational changes were observed during the simulation. However, RMSF data revealed that the substitution of arginine at position 2032 reduces the overall flexibility of the protein (Fig. S4A). In particular, the mutant was highly stabilized by formation of a salt bridge between the guanidinium group of R2032 and the carboxyl group of β -strand residue E1961. Additionally, although simulations using native ROS1 revealed a hydrogen bond between residues R1948 and T1963, this interaction was lost in the G2032R mutant. Instead, R1948 of the mutant kinase reorients toward the ATP binding site,

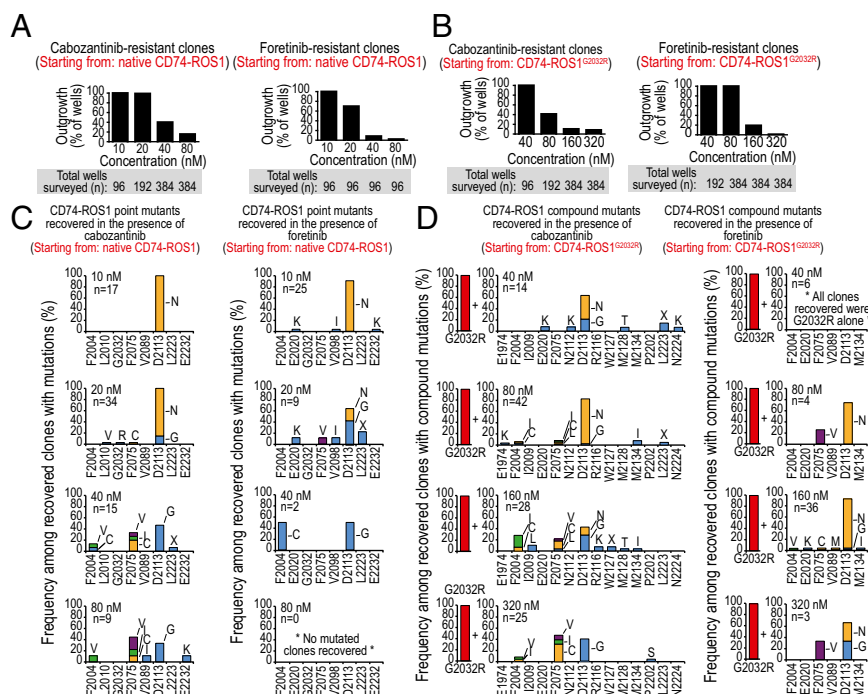


Fig. 4. In vitro mutagenesis screens suggest partially overlapping ROS1 point mutation and compound mutation resistance profiles for cabozantinib and foretinib. (A) Outgrowth summaries for cell-based resistance screens starting from Ba/F3 cells expressing native CD74-ROS1. (B) Outgrowth summaries for cell-based resistance screens starting from Ba/F3 CD74-ROS1^{G2032R} cells. Breakdowns of frequency and spectra of mutant clones recovered in the presence of increasing concentrations of cabozantinib and foretinib are shown for assays starting from (C) native CD74-ROS1 and (D) CD74-ROS1^{G2032R} cells. The number of clones sequenced for each condition is indicated, and multiple substitutions at a single position are indicated as stacked bars.

forming an unusual ion-pair with R2032 that restricts P-loop flexibility. This interaction, although uncommon, has also been observed in other proteins as a stabilizing factor (26–28).

To overcome challenges associated with incorporating receptor flexibility into computational analysis of inhibitor binding mode and strength (29), we performed docking assessment on the entire conformational ensemble generated by the MD simulation (30). Consistent with the high degree of resistance conferred by the ROS1^{G2032R} mutant to crizotinib, modeling showed that R2032 forms stable interactions that result in partial occupancy of the crizotinib-binding site, creating a direct steric clash between the guanidinium group of R2032 and the pyrazole and piperidine moieties of crizotinib. Additional stabilization and reorientation of residues such as L1951 also constrict the piperidine-binding region. Docking simulations performed on the native ROS1 MD ensemble accurately predicted the crizotinib binding pose (most favorable docking score of -9.6 kcal/mol; systems with a score less than -6 kcal/mol are empirically categorized as good binders), as solved previously by X-ray crystal structure (22) (Fig. 2D). Docking simulations also distinguished the capacity for crizotinib binding between native ROS1 and ROS1^{G2032R}, displaying poor docking scores for the G2032R mutant (Fig. 2E). In contrast, docking of cabozantinib and foretinib resulted in good binding scores for both native ROS1 and ROS1^{G2032R} (Fig. 2E), again consistent with in vitro results. Crizotinib resistance is mainly attributable to steric incompatibility between the partially solvated piperidine moiety of crizotinib and the arginine sidechain of residue 2032. By contrast, the quinoline group of cabozantinib is positioned at a substantial distance from the arginine side chain of residue 2032, leaving sufficient space for this residue to engage in a salt bridge with E1961. This positioning was evident upon inspection of the docked poses of cabozantinib, which suggest that the quinoline moiety of cabozantinib is positioned at least 5 Å away from the R2032 side chain. These findings extend our understanding of how the

G2032R mutant confers crizotinib resistance (22) and confirm the ability of computational modeling to accurately predict the binding selectivity of ROS1 TKIs.

The ROS1-Selective TKIs Cabozantinib and Foretinib Bind the Inactive Conformation of ROS1. Small-molecule, ATP-competitive TKIs generally engage with a target kinase in a type I or type II manner, corresponding to binding of the catalytically active or inactive conformation, respectively. Analysis of the binding pose of cabozantinib in complex with ROS1 demonstrated a preference for the inactive conformation, with the lowest docking score being -12 kcal/mol (Fig. 3A). Specifically, the quinoline moiety of cabozantinib was found to occupy the adenine-binding site, forming a hydrogen bond with the backbone atoms of E2027 and M2029, whereas the aryl linker makes aromatic stacking interactions with F2103 of the DFG motif (Fig. 3B). This observation is further affirmed by the fact that a number of crystal structures of kinases bound with quinolone- or quinazoline-based inhibitors showed that these fragments specifically occupy the adenine-binding site (31–33). Additional interactions include a hydrogen bond between the dicarboxamide group of cabozantinib (positioned close to gatekeeper residue L2026) and the catalytic K1980 residue and engagement of the fluorophenyl moiety (occupying the specificity site) with F2004 and F2075 in T-shaped and π - π aromatic stacking, respectively. Residues lining the specificity site (M2001, L2070, and I2100) provide additional hydrophobic interactions between cabozantinib and ROS1.

To understand whether ROS1 displays an induced effect upon cabozantinib binding, the ROS1:cabozantinib complex with the lowest docking score was subjected to MD simulation for 50 ns under explicit solvent conditions, and the resulting trajectory was analyzed after stripping the solvent and the ligand molecule. Subsequent redocking of cabozantinib to the MD ensemble generated from this holo-simulation revealed dramatically more

favorable binding than the parent apo-simulation conformation from which it was initialized, improving the docking score to -16 kcal/mol and strongly suggesting induced conformational changes at the binding site (Fig. 3C). MD simulation of the complex facilitates relaxation of the enzyme and ligand by removing any close contacts or strain observed in the initial docked pose. Subtle changes in the orientation and displacement of both the structural moieties of the cabozantinib molecule and the residues within 4 Å of cabozantinib significantly improved the binding score. For example, the dicarboxamide and cyclopropyl moieties of cabozantinib were in close contact with residues D2102 and E1997 in the apo-simulated docking pose. Repositioning of these amino acids and neighboring residues resulted in optimized hydrogen bonding with the dicarboxamide group as well as more favorable van der Waals interactions between the fluorophenyl group and specificity site residues L2070 and I2100. Also, slight readjustment in the position of the quinoline moiety of cabozantinib relaxed a close contact with residue L1951 observed in the starting point docked pose.

Foretinib, a close structural analog of cabozantinib (Table 1), was also docked to the ROS1 MD conformational ensemble. Analysis of the foretinib-docking pose showed a similar cabozantinib-like binding mode, with the additional morpholine moiety in foretinib interacting with residues K1976 and E2030 (Fig. 3B). This docking pose is further supported by the c-MET crystal structure bound with foretinib, which showed a similar binding conformation (34). However, closer examination of the foretinib docked poses additionally revealed a reverse binding pose, wherein the morpholine group formed favorable interactions with the α C-helix, whereas the fluorophenyl and quinoline moieties instead occupy the adenine-binding site and specificity site, respectively (Fig. 3B). Although intriguing, such inhibitor alternative-binding modes have also been visualized in other kinases (35, 36). For example, the crystal structure of SYK kinase revealed an alternate binding pose for imatinib (PDB ID code 1XBB). Examination of the top 200 conformations confirmed that $\sim 68\%$ of

the docked poses maintained the cabozantinib-like pose whereas $\sim 32\%$ exhibited the reverse binding mode. Based on this putative dual binding mode capacity for foretinib but not cabozantinib, we generated Ba/F3 CD74-ROS1 cell lines with alanine substitutions at select positions predicted from the modeling to preferentially disturb cabozantinib binding versus foretinib reverse pose binding. Accordingly, all four alanine mutants tested demonstrated ~ 2.5 -fold to fivefold decreased sensitivity to cabozantinib compared with foretinib in vitro (Fig. 3D). This discovery suggests that foretinib may potentially engage the kinase in its reverse binding mode upon mutation although more rigorous free energy calculations would be necessary to ascertain this finding. Overall, these findings suggest that ROS1-selective TKIs bind to the inactive conformation of ROS1 in a type II manner, in contrast to the type I binding mode exhibited by the dual ROS1/ALK inhibitor crizotinib.

ROS1-Selective TKIs Feature Largely Distinct Resistance Profiles Compared with Dual ROS1/ALK Inhibitors. Acquired TKI resistance due to point mutations is a frequent clinical challenge in many malignancies, including NSCLC (37–39). Given our findings that, among the inhibitors tested, the ROS1-selective TKIs cabozantinib and foretinib uniquely retain potent activity against the CD74-ROS1^{G2032R} mutant, we prospectively investigated potential mutations capable of conferring resistance to either or both TKIs. Accelerated cell-based resistance screens were performed starting from Ba/F3 cells expressing native CD74-ROS1 in the presence of increasing concentrations of cabozantinib or foretinib. We observed a concentration-dependent reduction in the percentage of wells that exhibited outgrowth with each TKI (Fig. 4A and Table S2). For both TKIs, sequencing of recovered clones for ROS1 kinase domain mutations revealed position 2113 in the A-loop as the most frequently mutated residue at all concentrations tested. The specific substitution at this position shifted from asparagine to glycine with increased TKI concentrations (Fig. 4C). With respect

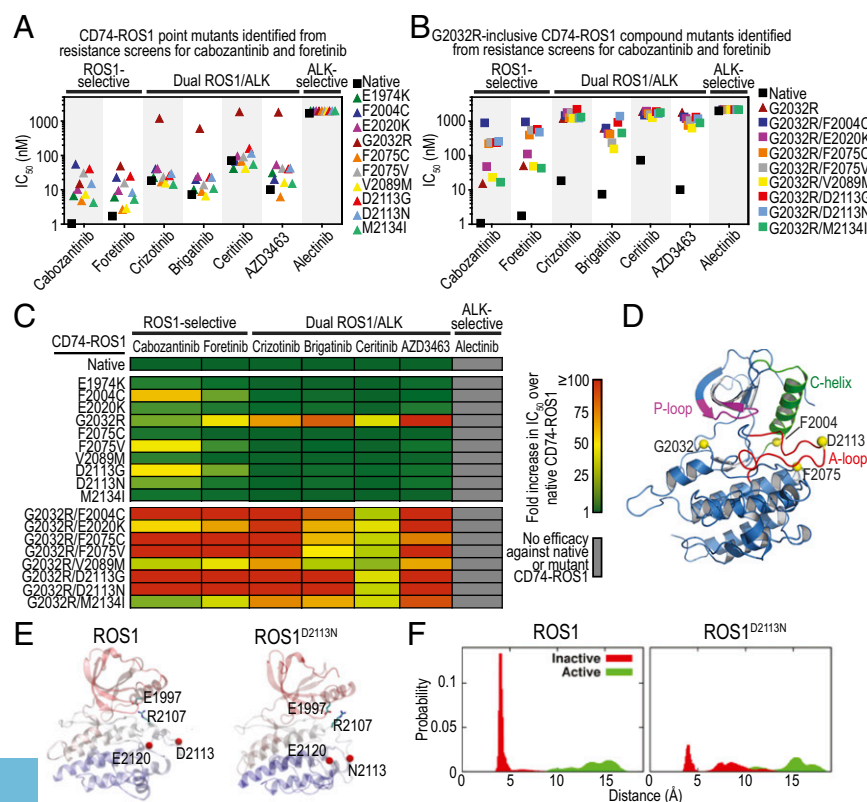


Fig. 5. Mutants recovered from resistance screens for ROS1-selective TKIs, including those involving position D2113, confer varying levels of sensitivity to dual ROS1/ALK inhibitors. Scatter plots of cell proliferation IC_{50} s for the indicated TKIs are shown for Ba/F3 cells expressing (A) CD74-ROS1 point mutations and (B) G2032R-inclusive CD74-ROS1 compound mutations recovered in resistance screens for foretinib and cabozantinib. (C) Heat map depicting differential levels of sensitivity of the CD74-ROS1 point mutations and G2032R-inclusive compound mutations discovered from resistance screens. The indicated color gradient represents fold increase over IC_{50} for native CD74-ROS1 cells. (D) Ribbon structure description of the inactive ROS1 kinase domain, highlighting four positions implicated in TKI resistance and showing the C_{α} atom in van der Waals representation. The structural elements of the P-loop (magenta), A-loop (red), and α C-helix (green) are highlighted. (E) Predicted structural consequence of the ROS1^{D2113N} mutation. Positions 2113 and 2120, which form a unique salt-bridge in the mutant kinase (Right), are shown as red balls. The two residues used to evaluate effects of the mutation on the A-loop (R2107) and α C-helix (E1997) are shown as sidechains in monitoring the shift of the activation loop to resemble a more type I-like conformation in the mutant. (F) A-loop: α C-helix-correlated conformational shift as measured by distance profiles from simulation of the active and inactive states of native ROS1 and ROS1^{D2113N}.

to cabozantinib, multiple substitutions of residues F2004 [cysteine (C)/valine (V)] and F2075 [cysteine (C)/isoleucine (I)/valine (V)] were recovered from concentrations up to 80 nM, consistent with favorable interactions between the fluorophenyl group of the inhibitor and these residues implicated from computational modeling of cabozantinib binding (Figs. 3B and 4C). Also in line with predictions from modeling of variant foretinib binding poses, mutations at these two positions were recovered less frequently with foretinib than cabozantinib (Fig. 4C and Table S2). Notably, the F2075V mutation of ROS1 is analogous to the F359V mutation in the kinase domain of ABL1, which is known to confer high-level resistance to imatinib and nilotinib, both of which bind an inactive conformation of the kinase (see Fig. S6) (40).

A more recent issue that has gained attention in molecularly targeted kinase inhibitor therapies is the risk for acquiring multi-drug-resistant compound mutations as an undesirable byproduct of sequential TKI therapy (41–43). Given cabozantinib's efficacy against the crizotinib-resistant CD74-ROS1^{G2032R} mutant, a fraction of patients treated with second-line cabozantinib may harbor G2032R or another mutation at baseline. To anticipate G2032R-inclusive ROS1 compound mutations that may confer resistance to ROS1-selective TKIs, we performed resistance screens starting from Ba/F3 CD74-ROS1^{G2032R} cells in the presence of cabozantinib or foretinib (Fig. 4B). Similar to screens starting from native CD74-ROS1, we observed a concentration-dependent reduction in the number of wells with outgrowth and the spectrum of mutated residues. Low frequency mutations identified in resistant clones recovered from cabozantinib-treated wells included the following: E1974K, I2009L, E2020K, N2112K, R2116K, W2127*, M2128T, M2134I, L2223*, and N2224K (Fig. 4D and Table S3). Position 2113 was the most frequently mutated site in tandem with G2032R for both TKIs, with clones recovered at concentrations as high as 320 nM for foretinib and 640 nM for cabozantinib largely constricting to compound mutants pairing G2032R with F2004(I/V/C), F2075(C/I/V), or D2113G (Fig. 4D and Table S3).

To evaluate the sensitivity of mutations identified in our resistance screens for cabozantinib and foretinib to other ROS1 TKIs, we rederived nine of the most frequently recovered single mutants (E1974K, F2004C, E2020K, F2075C, F2075V, V2089M, D2113G, D2113N, and M2134I) and eight G2032R-inclusive compound mutations (G2032R paired with F2004C, E2020K, F2075C, F2075V, V2089M, D2113G, D2113N, or M2134I) in Ba/F3 CD74-ROS1 cells and tested their sensitivity against our panel of seven TKIs (Fig. 5 A and B and Table S4). All single mutants showed 2- to 30-fold decreased sensitivity to the ROS1-selective, type II inhibitors, cabozantinib and foretinib, but remained sensitive to the dual ROS1/ALK, putative type I binders crizotinib, brigatinib, ceritinib, and AZD3463. Consistent with the insensitivity of the CD74-ROS1^{G2032R} mutant to all of the tested dual ROS1/ALK TKIs, we found that all G2032R-inclusive ROS1 compound mutants also exhibit high-level resistance. By contrast, G2032R-inclusive CD74-ROS1 compound mutants displayed varying degrees of resistance to cabozantinib and foretinib. For example, among the most frequently recovered compound mutations for cabozantinib was G2032R/D2113N (Fig. 4D and Table S3), which demonstrated ~15-fold increased IC₅₀ (255.8 nM) for cabozantinib, compared with cells expressing G2032R or D2113N (Fig. 5 A and B and Table S4). Overall, results from profiling of single mutants suggest that, whereas ROS1 kinase domain point mutations involving residues F2004, F2075, and D2113 may confer resistance to the ROS1-selective inhibitors cabozantinib and foretinib, they may remain sensitive to dual ROS1/ALK TKIs. However, emergence of compound mutations poses a potential vulnerability for both of these categories of ROS1 TKIs (Fig. 5 C and D).

The ROS1^{D2113N} Mutant Induces an Altered A-Loop Conformation and Compromises Binding of Cabozantinib. Given the high frequency with which the D2113N mutation was recovered from cell-based

resistance screens for CD74-ROS1, we performed MD simulations of this mutant to elucidate the local and global conformational changes induced in the ROS1 kinase domain. RMSF analysis of the ROS1^{D2113N} inactive conformation showed decreased flexibility of the A-loop compared with native ROS1 (Fig. S4B). This altered flexibility can be attributed to the local changes observed in the A-loop upon mutation, indirectly impacting the binding site of ROS1-selective TKIs. The D2113 residue in native ROS1 simultaneously interacts with the positively charged R2116 and is repelled by another negatively charged residue in the A-loop (E2120). The D2113N mutation nullifies this repulsion and instead creates a hydrogen bond between these two residues (N2113 and E2120) (Fig. 5E), resulting in a significant shift and stabilization of the ROS1^{D2113N} A-loop conformation and alteration of the α C-helix dynamics.

To investigate the dynamics of the α C-helix relative to the A-loop, the distance between residue E1997 (α C-helix) and R2107 (A-loop) was monitored throughout the MD simulation. Notably, these residues are proximal and form a salt bridge in the inactive kinase, as observed in many other kinases adopting an SRC-like inactive conformation (44–46), whereas they are further apart and lack such interaction in the active state (Fig. 5E). Although distance profiling of the active conformation from MD simulation showed that both ROS1 and ROS1^{D2113N} sampled similarly (14 and 15 Å, respectively) (Fig. 5F), conformational analysis of the inactive state showed a bimodal distribution, with higher distances for ROS1^{D2113N} (averaged at 4.8 and 8.5 Å) compared with native ROS1 (4 Å). These data suggest that the inactive state of native ROS1 participates in salt bridge formation between E1997 and R2107 (as inferred from the reduced distance between them) and that the D2113N mutant displaces R2107 outside of the α C-helix and the interaction between E1997 and R2107 is lost. Due to displacement of residue R2107 in ROS1^{D2113N}, E1997 reorients its sidechain and partially occupies the specificity site, thereby creating a potential steric clash with type II binding inhibitors. Although alterations in the specificity pocket due to the D2113N mutation present a possible resistance mechanism scenario for type II inhibitors, inherent limitations in the initialization of the computational model or the finite accessibility of the simulation time scales cannot be completely ruled out.

Foretinib and cabozantinib were docked to the inactive ROS1^{D2113N} MD ensemble and compared with native ROS1. We found that both inhibitors demonstrated significantly less favorable docking scores for ROS1^{D2113N} (Fig. S5) compared with native ROS1. In contrast, crizotinib demonstrated equivalent, favorable docking scores for both native ROS1 and ROS1^{D2113N} (Fig. S5). Taken together, these results suggest that alterations of position D2113 may represent a unique liability for ROS1-selective type II inhibitors, possibly impacting the conformation of the specificity site. Although speculative in nature, relevant experiments are warranted to further explore these differences.

Discussion

Rational, molecularly guided clinical use of TKI therapies has substantially impacted patient outcomes in several cancer subtypes, including NSCLC (37, 47). The recent establishment of rearranged *ALK* and *ROS1* as distinct molecular diagnostic subgroups of NSCLC, coupled with the clinical efficacy of crizotinib, has driven an explosion of new inhibitor development. Although several inhibitors have shown promising clinical activity (48–50), resistance to therapy has already surfaced. The high degree of sequence homology between the catalytic domains of *ALK* and *ROS1* suggests that *ALK* TKIs may be repurposed as *ROS1* inhibitors and vice versa, but our results establish limits to this inhibitor design principle.

Upon consideration of all available results for first- and second-generation *ALK* and/or *ROS1* TKIs, including the current study, we suggest three operational categories of selectivity: dual ROS1/

ALK, ROS1-selective, and ALK-selective. Among the dual ROS1/ALK TKIs, crizotinib and ceritinib both demonstrate crystallographic evidence of a type I binding mode for ALK, and a similar binding mode is observed for the ROS1:crizotinib complex (22, 51, 52). Our computational studies reveal considerably greater structural similarity between the catalytically active conformations of ALK and ROS1, and the chemical scaffolds of the newer dual ROS1/ALK TKIs ceritinib, brigatinib, and AZD3463 are highly related (Table 1), suggesting a common preferential type I binding mode among dual ROS1/ALK inhibitors. Intriguingly, the ALK-selective inhibitor alectinib, which exhibits no ROS1 inhibitory activity, has also been reported to preferentially engage the active conformation of ALK (53). Modeling of alectinib in active ALK suggests that this lack of activity against ROS1 is due at least in part to two interactions not present in ROS1: (i) interaction of the ethyl group of alectinib with a hydrophobic ALK hinge region residue (A1200) and (ii) unique access of alectinib's nitrile group to the specificity site (despite its type I binding mode) by interacting with E1167 of the ALK α -helix. Notably, this analysis may also provide additional context for understanding the mechanism behind the reported alectinib-resistant ALK^{V180L} mutation (54), which is predicted to disrupt this nitrile-E1167 interaction.

In contrast, the ROS1-selective inhibitors cabozantinib and foretinib exhibit a type II binding mode and preferentially engage the inactive conformation of ROS1. This binding mode is primarily due to structurally important differences that permit accommodation of larger, type II inhibitor scaffolds. It is known that, in comparison with the specificity site of the inactive kinase domain, the ATP binding site in the active conformation is highly conserved among many kinases, forming the basis of selective type II inhibitor design (55). Notably, we observed that cabozantinib binding to ROS1 involves conformational selection, followed by an induced-fit mechanism to achieve optimized interaction. A recent study by Wilson et al. used an evolutionary approach to examine protein structure and identified a similar induced-fit mechanism for imatinib that is critical to its selective type II binding of ABL1 compared with the highly related SRC kinase (56). Such a binding mechanism may also have implications for additional biochemical properties, including kinetic on- and off-rates. Although our ensemble docking of the structurally related foretinib showed a similar initial binding pose to that of cabozantinib, an alternate reverse orientation binding mode was also present. Conformational clustering revealed that the reverse binding mode exhibited by foretinib was present primarily in low-population clusters featuring a slightly more open specificity site. Further studies using free energy calculations and advanced sampling methods will be required for in depth characterization. Together, these findings suggest a potentially important theme in application of small-molecule TKI therapies, wherein structural differences in the inactive conformations of related kinases may explain both the mechanistic subtleties and the contrasts seen in TKI binding affinity and inhibitory efficacy (56, 57).

Consistent with differences in binding mode, distinct patterns of kinase domain point mutation-based resistance are apparent for the three categories of TKIs described here. In ALK-rearranged NSCLC, crizotinib resistance due to acquisition of kinase domain mutations is routinely observed, with 11 substitutions spanning 9 residues reported in clinical resistance (Table 1), in addition to several other residues implicated from in vitro resistance screening assays (20, 21). Although clinical follow-up remains limited for the newer inhibitors, a subset of crizotinib-resistant ALK mutations (those involving positions 1171, 1174, and 1202) have already been implicated in clinical resistance to the dual ROS1/ALK TKI ceritinib and/or the ALK-selective TKI alectinib (Table 1) (21, 54, 58). This pattern is akin to the clinical experience in EGFR-driven lung cancer, where type I TKIs such as erlotinib evoke dramatic but inevitably transient responses, funneling to common point mutation-based failure (47). Although newer EGFR TKIs with different

binding properties (e.g., irreversible binding, such as afatinib) have offered some benefit, resistance and/or intolerance is still commonly observed. The only reported ROS1 mutation in clinical resistance to date is CD74-ROS1^{G2032R} (analogous to the resistant G1202R mutation found in EML4-ALK) (Fig. S6), verified at autopsy in a patient with metastatic NSCLC that had been controlled with crizotinib before relapse (22). Our finding that this mutation remains highly sensitive to cabozantinib is consistent with a recent report (59). Given cabozantinib's efficacy against both native and G2032R-mutant ROS1 fusions, an investigational new drug filing with the FDA for evaluation of cabozantinib in crizotinib-naive and -refractory ROS1 fusion-positive lung cancer has been initiated (clinical trial identifier, NCT01639508), and a phase 2 trial is actively accruing patients (clinical trial identifier, NCT01639508).

Clinical experience with TKIs for ROS1- and ALK-driven NSCLC, along with our in vitro profiling and structural modeling data, suggests important themes regarding resistance. First, with respect to dual ROS1/ALK inhibitors (type I mode binders), ROS1 mutations within the ATP binding site may represent a significant resistance liability. All tested TKIs in this category demonstrated limited to no efficacy against cells expressing the CD74-ROS1^{G2032R} mutant (Fig. 2A and B). Conversely, ROS1-selective inhibitors (type II mode binders) remain highly effective against ATP binding site mutations but are vulnerable to variants that favor the active conformation of ROS1 or those that constrict the specificity site of inactive ROS1. As an example, mutations at the F2004 and F2075 sites of ROS1 reside in the specificity pocket, which is occupied by the type II inhibitors cabozantinib and foretinib, but usually not by type I compounds. The nearly nonoverlapping resistance profiles of type I compared with type II inhibitors may open an important strategy for clinical management of resistance.

Dual ROS1/ALK TKIs remain effective against nearly all mutations in the specificity site that confer resistance to the ROS1-selective inhibitors. However, in line with findings from sequential therapy with ABL1 TKIs in CML (41–43), the potential emergence of G2032R-inclusive compound mutations in ROS1 fusions could yield high-level resistance to multiple type I and type II inhibitors (Fig. 5B and C). At present, it is not known whether the ROS1^{G2032R} mutation detected in a relapsed patient will be the most prevalent resistance mutation for ROS1. Although the overall median duration of responses to crizotinib in ROS1 fusion-positive patients seems longer than that observed in patients harboring ALK fusions (15), resistance profiles are still nascent and will take several years of clinical experience to fully establish. Nonetheless, the spectrum of ROS1 TKI-resistant mutations implicated clinically or from cell-based screening to date is noticeably restricted, compared with results from similar profiling of ABL1 TKIs in CML (60, 61), suggesting a scenario more like that seen with FLT3 TKIs in acute myeloid leukemia (62), where escape routes are confined to a relatively smaller set of mutations. This finding has potential implications for continued TKI development and the prospect of maximal control of ROS1 mutation-mediated drug resistance. In addition to the activity of ROS1 inhibitors, clinical tolerability in the face of chronic dosing will likewise serve as an important determinant of how and in what order to effectively use these treatments in the clinic. These clinical decisions may also ultimately dictate the durability of response and emergence of TKI-resistant mutations.

Looking forward, consideration should be given to development of new inhibitors for ROS1 and ALK. One possibility is to develop and optimize type II inhibitors for ALK. Although a preclinical type II ALK scaffold has been described (63), to our knowledge, there are no reported clinical TKIs that engage the inactive conformation of ALK. Whether such TKIs would demonstrate differential efficacy over their type I binding counterparts remains to be seen although the possibility of a nonoverlapping resistance profile might offer additional options for patients with refractory

ALK-rearranged disease. Another important consideration for TKI development is that, although targeting both ROS1 and ALK with a single drug may seem appealing in terms of broader clinical applicability, attempting to target resistance mutations within the active conformation TKI binding sites, such as G1202R in ALK and G2032R in ROS1, may prove difficult given overlapping resistance profiles of such type I inhibitors. Alternatively, structure-based design of improved, potent ROS1-selective TKIs that accommodate mutations, either by avoiding direct contact with such residues or by using additional productive contacts within the altered binding pocket, may prove a useful strategy.

In summary, our *in vitro* profiling of a panel of clinical TKIs, combined with computational structural modeling and resistance screening, helps define therapeutically relevant differences between ROS1 and ALK, providing a basis for further development of inhibitors to circumvent resistance in NSCLC and other malignancies.

Methods

Cell Viability Assays. All TKIs were prepared as 1-mM stocks in DMSO before each experiment. Inhibitors were distributed at 2× concentration using a D300 Digital Dispenser (HP) [capable of accurately administering very small volumes (10 pL–150 nL)] into 384-well plates preloaded with 25 μ L per well of complete medium. Ba/F3 cells expressing CD74-ROS1 constructs were seeded (800 cells per well; 25 μ L) into drug plates using a Multidrop Combi Reagent Dispenser (Thermo Scientific), and plates were incubated for 72 h at 37 °C, 5% CO₂. Viability was measured using a methanethiosulfonate-based assay (CellTiter96 Aqueous One Solution; Promega) read on a Biotek Synergy 2 plate reader. All experiments were performed at least two independent times in triplicate. Data were normalized using Microsoft Excel, and absolute IC₅₀ values were calculated with GraphPad Prism software using a nonlinear curve fit equation modified using previously described parameters (64).

Immunoblot Analysis. Ba/F3 CD74-ROS1, CD74-ROS1^{G2032R}, and EML4-ALK cells, as well as human NSCLC cell lines (HCC78 and H3122), were treated with the indicated concentrations of inhibitors for 2 h, pelleted, washed once in ice-cold PBS, and lysed in 200 μ L of cell lysis buffer (Cell Signaling Technology) supplemented with 0.25% deoxycholate, 0.05% SDS, and protease and phosphatase inhibitors. Equal amounts of protein were extracted with SDS sample buffer for 15 min at 80 °C and run on 4–15% Tris-glycine precast gradient gels (Criterion; Bio-Rad). Proteins were transferred to Immobilon-FL membranes (Millipore) and probed with phospho-ROS1 [3078, 1:1,000; Cell Signaling Technology (CST)], total ROS1 (3266, 1:1,000; CST), phospho-ERK1/2 (9101, 1:1,000; CST), total ERK2 (sc-1647, 1:2,000; Santa Cruz), total ALK (3333, 1:1,000; CST), phospho-ALK (6941, 1:1,000; CST), phospho-Akt (4060, 1:1,000; CST), AKT (610860, 1:1,000; BD Transduction Laboratories), and GAPDH (AM4300, 1:5,000; Ambion). Blots were imaged using either a LI-COR Odyssey imaging system or the Bio-Rad ChemiDoc imaging station according to the manufacturer's protocol for immunoblot detection with use of infrared dye or horseradish peroxidase-conjugated secondary antibodies, respectively.

Accelerated Cell-Based Resistance Screen. Ba/F3 cells expressing native CD74-ROS1 or CD74-ROS1^{G2032R} were treated overnight with *N*-ethyl-*N*-nitrosourea (ENU) (50 μ g/mL), pelleted, washed, resuspended in fresh media, and distributed into 96-well plates (1 × 10⁵ cells per well) in 200 μ L of complete medium supplemented with the indicated concentrations of either cabozantinib or foretinib. Wells were observed for media color change and cell growth under an inverted microscope daily for 4 wk, and wells exhibiting outgrowth were transferred to 24-well plates containing 2 mL of complete medium supplemented with the same concentration of cabozantinib or foretinib. At confluency, these wells were harvested, pelleted, and stored at –20 °C. Genomic DNA was extracted using a DNeasy Tissue Kit (Qiagen); for low inhibitor concentrations wherein near 100% outgrowth of wells was observed, DNA was extracted from a randomly selected subset of expanded clones. The CD74-ROS1 kinase domain was amplified using primers CD74-ROS1 M13F1 (5'-GTA AAA CGA CGG CCA GTG CTC TTC CAA CCC AAG AGG-3') and ROS1-M13Kin1-Rev1 (5'-CAG GAA ACA GCT ATG ACC GCC ATC TTC ACC TTC AAA GC-3') and bidirectionally sequenced using M13F (5'-GTA AAA CGA CGG CCA GTG-3') and M13R primers (5'-CAG GAA ACA GCT ATG ACC-3'). The resultant chromatographs were analyzed for mutations using Mutation Surveyor software (SoftGenetics).

Molecular Dynamics Simulations. Molecular dynamics (MD) simulation was performed using the Amber ff12SB force field (65) in NAMD simulation software (66). During the initial stages of model refinement, nonhydrogen atoms were restrained (100 kcal/mol/Å²), and the system was relaxed by energy minimization using 1,000 steps of the steepest descent algorithm. During the next stages of the heating, equilibration, and production run, all bonds involving hydrogen atoms were restrained using the SHAKE algorithm (67). Periodic boundary conditions with particle mesh Ewald summation were used to handle the long-range electrostatic interactions (real-space truncation at 9.0 Å and grid spacing of 1.0 Å) (68). All eight systems were heated from 100 to 300 K in 50 ps using a 1-fs time-step. After heating of all systems, 5 ns of equilibration were performed using the NPT ensemble with a 2-fs time-step. Temperature and pressure were controlled at 300 K and 1 atm using the Nosé-Hoover Langevin piston algorithm (69) and Langevin dynamics (70), respectively. For each of the eight systems, three independent replicates were generated and simulated for 500 ns using the NPT ensemble. Coordinates were saved every 10 ps, and conformational analysis was performed on the combined ensemble. A cumulative 12 μ s simulation trajectory was generated for further analysis.

Conformational Analysis of ROS1 and ALK. The CPPTRAJ software of the AmberTools suite was used for postprocessing the MD-generated trajectories (71). For each system, a combined 1,500-ns (500 ns and three replicates) trajectory was analyzed for various molecular properties. Root mean square deviation (rmsd) and root mean square fluctuation (RMSF) of the protein were measured using a trajectory fitted on either the initial or average structure as reference. Structural fitting was performed using a least-square fitting method for the protein backbone atoms. Rotation of the α -C-helix was estimated using an angle defined by the C α atoms of three residues located in the N and C terminus of the α -C-helix and the rigid F-helix: Q1989, F2004, and W2145 for ROS1 and the corresponding residues in ALK (Q1159, F1174, and W1313). The specificity site pocket volume of ROS1 and ALK was measured using the POVME program (72), with both kinases' trajectories aligned using the binding site as defined by the following residues: L1951, A1978, K1980, E1997, M2001, L2028, G2032, L2086, and D2102 for ROS1 and equivalent residues in ALK based on structural alignment. This qualitative estimate of the pocket volume is independent of the definition of the active site used here for alignment. Interatomic distances between residues in the P-loop (F1956), α -C-helix (E1997), and A-loop (R2107) of ROS1 and ALK (corresponding residues) were measured using the position of the C α atoms during the course of the simulation.

Molecular Docking Simulations. Ensemble docking was performed using the Glide program of Schrödinger's package (Suite 2012, Maestro, version 9.3). Conformations (1,500) were extracted from each simulated system (one conformation for every nanosecond), and a docking grid for the receptor was generated using the binding site residues defined above (encompassing the ATP binding site and specificity site). Ligands (crizotinib, foretinib, cabozantinib, and alectinib) were prepared using the Ligprep module of the Schrödinger's package (version 3), docked using the GlideXP method (Glide version 5.8; Schrödinger, LLC), and analyzed for binding interactions (73). Parameterization of cabozantinib was performed using standard Amber protocol (74). Cabozantinib geometry was optimized using Gaussian 09 (www.gaussian.com) at the HF/6-31G* level theory consistent with ff12SB force fields, and initial atomic charges were derived using restricted electrostatic potential (RESP) (75). Fifty nanoseconds of implicit solvent generalized-Born MD simulation was performed at 300 K, and the resulting trajectory was clustered using the CPPTRAJ program (71). Representative structures from the top three clusters were selected, and the geometry was optimized at the HF/6-31G* level. RESP charges were derived using the multiconformation charge fitting method. Antechamber was used to assign other parameters from the generalized Amber force field (74).

ACKNOWLEDGMENTS. We thank Matthew Zabriskie for technical assistance and members of the B.J.D., M.W.D., and T.O. laboratories for valuable discussion. M.W.D. receives research funding from Bristol-Myers Squibb, Celgene, Novartis, and Gilead. This work was supported by the Howard Hughes Medical Institute (B.J.D.), and B.J.D. is supported by NIH Method to Extend Research in Time Award R37CA065823. M.A.D. is supported by a Hyundai Scholar Hope Grant. M.W.D. is supported by NIH Grants HL082978-01, 5 P01 CA049639-23, and R01 CA178397-01. T.O. is supported by NIH Grant R01 CA178397-01. N.A.V. acknowledges generous support from the Center for High Performance Computing (The University of Utah) and computing allocations at the Extreme Science and Engineering Discovery Environment (XSEDE) supercomputers (Award TG-CHE120086). XSEDE is supported by National Science Foundation Grant OCI-1053575.

1. Druker BJ (2009) Perspectives on the development of imatinib and the future of cancer research. *Nat Med* 15(10):1149–1152.

2. Druker BJ, et al.; IRIS Investigators (2006) Five-year follow-up of patients receiving imatinib for chronic myeloid leukemia. *N Engl J Med* 355(23):2408–2417.

3. Nowell PC, Hungerford DA (1960) Chromosome studies on normal and leukemic human leukocytes. *J Natl Cancer Inst* 25:85–109.
4. Shaw AT, Hsu PP, Awad MM, Engelman JA (2013) Tyrosine kinase gene rearrangements in epithelial malignancies. *Nat Rev Cancer* 13(11):772–787.
5. Grande E, Bolós MV, Arriola E (2011) Targeting oncogenic ALK: A promising strategy for cancer treatment. *Mol Cancer Ther* 10(4):569–579.
6. Awad MM, Shaw AT (2014) ALK inhibitors in non-small cell lung cancer: Crizotinib and beyond. *Clin Adv Hematol Oncol* 12(7):429–439.
7. Shaw AT, Engelman JA (2013) ALK in lung cancer: Past, present, and future. *J Clin Oncol* 31(8):1105–1111.
8. Davies KD, Doebele RC (2013) Molecular pathways: ROS1 fusion proteins in cancer. *Clin Cancer Res* 19(15):4040–4045.
9. Arai Y, et al. (2013) Mouse model for ROS1-rearranged lung cancer. *PLoS One* 8(2):e56010.
10. Charest A, et al. (2006) ROS fusion tyrosine kinase activates a SH2 domain-containing phosphatase-2-phosphatidylinositol 3-kinase/mammalian target of rapamycin signaling axis to form glioblastoma in mice. *Cancer Res* 66(15):7473–7481.
11. Saborowski A, et al. (2013) Mouse model of intrahepatic cholangiocarcinoma validates FIG-ROS as a potent fusion oncogene and therapeutic target. *Proc Natl Acad Sci USA* 110(48):19513–19518.
12. Bergethon K, et al. (2012) ROS1 rearrangements define a unique molecular class of lung cancers. *J Clin Oncol* 30(8):863–870.
13. Chin LP, Soo RA, Soong R, Ou SH (2012) Targeting ROS1 with anaplastic lymphoma kinase inhibitors: A promising therapeutic strategy for a newly defined molecular subset of non-small-cell lung cancer. *J Thorac Oncol* 7(11):1625–1630.
14. Shaw AT, et al. (2013) Crizotinib versus chemotherapy in advanced ALK-positive lung cancer. *N Engl J Med* 368(25):2385–2394.
15. Shaw AT, et al. (2014) Crizotinib in ROS1-rearranged non-small-cell lung cancer. *N Engl J Med* 371(21):1963–1971.
16. O'Hare T, Deininger MW, Eide CA, Clackson T, Druker BJ (2011) Targeting the BCR-ABL signaling pathway in therapy-resistant Philadelphia chromosome-positive leukemia. *Clin Cancer Res* 17(2):212–221.
17. Yu HA, Rieley GJ, Lovly CM (2014) Therapeutic strategies utilized in the setting of acquired resistance to EGFR tyrosine kinase inhibitors. *Clin Cancer Res* 20(23):5898–5907.
18. Rieley GJ, Politi KA, Miller VA, Pao W (2006) Update on epidermal growth factor receptor mutations in non-small cell lung cancer. *Clin Cancer Res* 12(24):7232–7241.
19. Doebele RC, et al. (2012) Mechanisms of resistance to crizotinib in patients with ALK gene rearranged non-small cell lung cancer. *Clin Cancer Res* 18(5):1472–1482.
20. Heuckmann JM, et al. (2011) ALK mutations conferring differential resistance to structurally diverse ALK inhibitors. *Clin Cancer Res* 17(23):7394–7401.
21. Lovly CM, Pao W (2012) Escaping ALK inhibition: Mechanisms of and strategies to overcome resistance. *Sci Transl Med* 4(120):120ps2.
22. Awad MM, et al. (2013) Acquired resistance to crizotinib from a mutation in CD74-ROS1. *N Engl J Med* 368(25):2395–2401.
23. Davare MA, et al. (2013) Foretinib is a potent inhibitor of oncogenic ROS1 fusion proteins. *Proc Natl Acad Sci USA* 110(48):19519–19524.
24. Baron R, McCammon JA (2013) Molecular recognition and ligand association. *Annu Rev Phys Chem* 64:151–175.
25. Dror RO, Dirks RM, Grossman JP, Xu H, Shaw DE (2012) Biomolecular simulation: A computational microscope for molecular biology. *Annu Rev Biophys* 41:429–452.
26. Magalhaes A, Maigret B, Hoflack J, Gomes JN, Scheraga HA (1994) Contribution of unusual arginine-arginine short-range interactions to stabilization and recognition in proteins. *J Protein Chem* 13(2):195–215.
27. Neves MA, Yeager M, Abagyan R (2012) Unusual arginine formations in protein function and assembly: Rings, strings, and stacks. *J Phys Chem B* 116(23):7006–7013.
28. Soetens J-CMC, Chipot C, Jansen G, Ángyán JG, Maigret B (1997) Effect of polarizability on the potential of mean force of two cations: The guanidinium-guanidinium ion pair in water. *J Phys Chem* 101(50):10910–10917.
29. Feixas F, Lindert S, Sinko W, McCammon JA (2014) Exploring the role of receptor flexibility in structure-based drug discovery. *Biophys Chem* 186:31–45.
30. Amaro RE, Baron R, McCammon JA (2008) An improved relaxed complex scheme for receptor flexibility in computer-aided drug design. *J Comput Aided Mol Des* 22(9):693–705.
31. Shewchuk L, et al. (2000) Binding mode of the 4-anilinoquinazoline class of protein kinase inhibitor: X-ray crystallographic studies of 4-anilinoquinazolines bound to cyclin-dependent kinase 2 and p38 kinase. *J Med Chem* 43(1):133–138.
32. Solomon VR, Lee H (2011) Quinoline as a privileged scaffold in cancer drug discovery. *Curr Med Chem* 18(11):1488–1508.
33. Zhang Q, et al. (2014) Identification of type II inhibitors targeting BRAF using privileged pharmacophores. *Chem Biol Drug Des* 83(1):27–36.
34. Qian F, et al. (2009) Inhibition of tumor cell growth, invasion, and metastasis by EXEL-2880 (XL880, GSK1363089), a novel inhibitor of HGF and VEGF receptor tyrosine kinases. *Cancer Res* 69(20):8009–8016.
35. Aronov AM, et al. (2007) Flipped out: Structure-guided design of selective pyrazolopyrrole ERK inhibitors. *J Med Chem* 50(6):1280–1287.
36. Atwell S, et al. (2004) A novel mode of Gleeev binding is revealed by the structure of spleen tyrosine kinase. *J Biol Chem* 279(53):55827–55832.
37. Camidge DR, Pao W, Sequist LV (2014) Acquired resistance to TKIs in solid tumours: Learning from lung cancer. *Nat Rev Clin Oncol* 11(8):473–481.
38. Choi YL, et al. (2010) ALK Lung Cancer Study Group (2010) EML4-ALK mutations in lung cancer that confer resistance to ALK inhibitors. *N Engl J Med* 363(18):1734–1739.
39. Chong CR, Jänne PA (2013) The quest to overcome resistance to EGFR-targeted therapies in cancer. *Nat Med* 19(11):1389–1400.
40. O'Hare T, et al. (2005) In vitro activity of Bcr-Abl inhibitors AMN107 and BMS-354825 against clinically relevant imatinib-resistant Abl kinase domain mutants. *Cancer Res* 65(11):4500–4505.
41. Shah NP, et al. (2007) Sequential ABL kinase inhibitor therapy selects for compound drug-resistant BCR-ABL mutations with altered oncogenic potency. *J Clin Invest* 117(9):2562–2569.
42. Soverini S, et al. (2013) Unraveling the complexity of tyrosine kinase inhibitor-resistant populations by ultra-deep sequencing of the BCR-ABL kinase domain. *Blood* 122(9):1634–1648.
43. Zabriskie MS, et al. (2014) BCR-ABL1 compound mutations combining key kinase domain positions confer clinical resistance to ponatinib in Ph chromosome-positive leukemia. *Cancer Cell* 26(3):428–442.
44. Levinson NM, et al. (2006) A Src-like inactive conformation in the abl tyrosine kinase domain. *PLoS Biol* 4(5):e144.
45. Shan Y, et al. (2009) A conserved protonation-dependent switch controls drug binding in the Abl kinase. *Proc Natl Acad Sci USA* 106(1):139–144.
46. Xu W, Doshi A, Lei M, Eck MJ, Harrison SC (1999) Crystal structures of c-Src reveal features of its autoinhibitory mechanism. *Mol Cell* 3(5):629–638.
47. Pao W, Chmielecki J (2010) Rational, biologically based treatment of EGFR-mutant non-small-cell lung cancer. *Nat Rev Cancer* 10(11):760–774.
48. Gadgeel SM, et al. (2014) Safety and activity of alectinib against systemic disease and brain metastases in patients with crizotinib-resistant ALK-rearranged non-small-cell lung cancer (AF-002JG): Results from the dose-finding portion of a phase 1/2 study. *Lancet Oncol* 15(10):1119–1128.
49. Gainer JF, et al. (2015) Alectinib salvages CNS relapses in ALK-positive lung cancer patients previously treated with crizotinib and ceritinib. *J Thorac Oncol* 10(2):232–236.
50. Shaw AT, et al. (2014) Ceritinib in ALK-rearranged non-small-cell lung cancer. *N Engl J Med* 370(13):1189–1197.
51. Cui JJ, et al. (2011) Structure based drug design of crizotinib (PF-02341066), a potent and selective dual inhibitor of mesenchymal-epithelial transition factor (c-MET) kinase and anaplastic lymphoma kinase (ALK). *J Med Chem* 54(18):6342–6363.
52. Friboulet L, et al. (2014) The ALK inhibitor ceritinib overcomes crizotinib resistance in non-small cell lung cancer. *Cancer Discov* 4(6):662–673.
53. Sakamoto H, et al. (2011) CH5424802, a selective ALK inhibitor capable of blocking the resistant gatekeeper mutant. *Cancer Cell* 19(5):679–690.
54. Katayama R, et al. (2014) Two novel ALK mutations mediate acquired resistance to the next-generation ALK inhibitor alectinib. *Clin Cancer Res* 20(22):5686–5696.
55. Davis MI, et al. (2011) Comprehensive analysis of kinase inhibitor selectivity. *Nat Biotechnol* 29(11):1046–1051.
56. Wilson C, et al. (2015) Kinase dynamics: Using ancient protein kinases to unravel a modern cancer drug's mechanism. *Science* 347(6224):882–886.
57. Zhao Z, et al. (2014) Exploration of type II binding mode: A privileged approach for kinase inhibitor focused drug discovery? *ACS Chem Biol* 9(6):1230–1241.
58. Lovly CM, et al. (2011) Insights into ALK-driven cancers revealed through development of novel ALK tyrosine kinase inhibitors. *Cancer Res* 71(14):4920–4931.
59. Katayama R, et al. (2015) Cabozantinib overcomes crizotinib resistance in ROS1 fusion-positive cancer. *Clin Cancer Res* 21(1):166–174.
60. Bradeen HA, et al. (2006) Comparison of imatinib mesylate, dasatinib (BMS-354825), and nilotinib (AMN107) in an N-ethyl-N-nitrosourea (ENU)-based mutagenesis screen: High efficacy of drug combinations. *Blood* 108(7):2332–2338.
61. O'Hare T, et al. (2009) AP24534, a pan-BCR-ABL inhibitor for chronic myeloid leukemia, potentially inhibits the T315I mutant and overcomes mutation-based resistance. *Cancer Cell* 16(5):401–412.
62. Smith CC, et al. (2012) Validation of ITD mutations in FLT3 as a therapeutic target in human acute myeloid leukaemia. *Nature* 485(7397):260–263.
63. Epstein LF, Chen H, Emkey R, Whittington DA (2012) The R1275Q neuroblastoma mutant and certain ATP-competitive inhibitors stabilize alternative activation loop conformations of anaplastic lymphoma kinase. *J Biol Chem* 287(44):37447–37457.
64. Sebaugh JL (2011) Guidelines for accurate EC50/IC50 estimation. *Pharm Stat* 10(2):128–134.
65. Case DA, et al. (2012) AMBER 12 (University of California, San Francisco).
66. Phillips JC, et al. (2005) Scalable molecular dynamics with NAMM. *J Comput Chem* 26(16):1781–1802.
67. Miyamoto S, Kollman PA (1992) Settle: An analytical version of the SHAKE and RATTLE algorithm for rigid water models. *J Comput Chem* 13(8):952–962.
68. Darden T, York D, Pedersen L (1993) Particle mesh Ewald: An N-log(N) method for Ewald sums in large systems. *J Chem Phys* 98(12):10089.
69. Martyna GJ, Tobias DJ, Klein ML (1994) Constant pressure molecular dynamics algorithms. *J Chem Phys* 101(5):4177.
70. Pastor RW, Brooks BR, Szabo A (1988) An analysis of the accuracy of Langevin and molecular dynamics algorithms. *Mol Phys* 65(6):1409–1419.
71. Roe DR, Cheatham TE (2013) PTRAJ and CPPTRAJ: Software for processing and analysis of molecular dynamics trajectory data. *J Chem Theory Comput* 9(7):3084–3095.
72. Durrant JD, Votapka L, Sørensen J, Amaro RE (2014) POVME 2.0: An enhanced tool for determining pocket shape and volume characteristics. *J Chem Theory Comput* 10(11):5047–5056.
73. Friesner RA, et al. (2006) Extra precision glide: Docking and scoring incorporating a model of hydrophobic enclosure for protein-ligand complexes. *J Med Chem* 49(21):6177–6196.
74. Wang J, Wolf RM, Caldwell JW, Kollman PA, Case DA (2004) Development and testing of a general amber force field. *J Comput Chem* 25(9):1157–1174.
75. Bayly C, Cieplak P, Cornell W, Kollman P (1993) A well-behaved electrostatic potential based method using charge restraints for deriving atomic charges: The RESP model. *J Phys Chem* 97(40):10269–10280.
76. Jorgensen WLCJ, Madura JD, Impey RW, Klein ML (1983) Comparison of simple potential functions for simulating liquid water. *J Chem Phys* 79:926.
77. Joong IS, Cheatham TE, 3rd (2008) Determination of alkali and halide monovalent ion parameters for use in explicitly solvated biomolecular simulations. *J Phys Chem B* 112(30):9020–9041.